

A Spectral Study of the Black Hole Candidate XTE J1752-223 in the High/Soft State with MAXI, Suzaku and Swift

Satoshi NAKAHIRA,¹ Shu KOYAMA,² Yoshihiro UEDA,³ Kazutaka YAMAOKA,⁴ Mutsumi SUGIZAKI,¹ Tatehiro MIHARA,¹ Masaru MATSUOKA,¹ Atsumasa YOSHIDA,⁴ Kazuo MAKISHIMA,^{1,5} Ken EBISAWA,⁶ Aya KUBOTA,⁷ Shin'ya YAMADA,⁸ Hitoshi NEGRO,⁹ Kazuo HIROI,³ Masaki ISHIKAWA,¹⁰ Nobuyuki KAWAI,¹¹ Masashi KIMURA,¹² Hiroki KITAYAMA,¹² Mitsuhiro KOHAMA,¹³ Takanori MATSUMURA,¹⁴ Mikio MORII,¹¹ Motoki NAKAJIMA,¹⁵ Motoko SERINO,¹ Megumi SHIDATSU,³ Tetsuya SOOTOME,^{1,7} Kousuke SUGIMORI,¹¹ Fumitoshi SUWA,⁹ Hiroshi TOMIDA,¹³ Yoko TSUBOI,¹⁴ Hiroshi TSUNEMI,¹² Shiro UENO,¹³ Ryuichi USUI,¹¹ Takayuki YAMAMOTO,^{1,9} Kyohei YAMAZAKI,¹⁴ Makoto S. TASHIRO,² Yukikatsu TERADA,² and Hiromi SETA²

¹MAXI team, Institute of Physical and Chemical Research (RIKEN), 2-1 Hirosawa, Wako, Saitama 351-0198

²Department of Physics, Saitama University, 255, Shimo-Okubo, Sakura-ku, Saitama 338-8570

³Department of Astronomy, Kyoto University, Oiwake-cho, Sakyo-ku, Kyoto 606-8502

⁴Department of Physics and Mathematics, Aoyama Gakuin University, 5-10-1 Fuchinobe, Chuo-ku, Sagamihara, Kanagawa 252-5258

⁵Department of Physics, The University of Tokyo, 7-3-1, Hongo, Bunkyo-ku, Tokyo, 113-0033

⁶Department of Space Science Information Analysis, Institute of Space and Astronautical Science, Japan Aerospace Exploration Agency, 3-1-1 Yoshino-dai, Chuo-ku, Sagamihara, Kanagawa 252-5210, Japan

⁷Department of Electronic Information Systems, Shibaura Institute of Technology, 307 Fukasaku, Minuma-ku, Saitama, Saitama 337-8570

⁸High Energy Astrophysics Laboratory, Institute of Physical and Chemical Research (RIKEN) 2-1 Hirosawa, Wako, Saitama 351-0198

⁹Department of Physics, Nihon University, 1-8-14, Kanda-Surugadai, Chiyoda-ku, Tokyo 101-8308

¹⁰School of Physical Science, Space and Astronautical Science, The graduate University for Advanced Studies (Sokendai), Yoshinodai 3-1-1, Chuo-ku, Sagamihara, Kanagawa 252-5210

¹¹Department of Physics, Tokyo Institute of Technology, 2-12-1 Ookayama, Meguro-ku, Tokyo 152-8551

¹²Department of Earth and Space Science, Osaka University, 1-1 Machikaneyama, Toyonaka, Osaka 560-0043

¹³ISS Science Project Office, Institute of Space and Astronautical Science (ISAS), Japan Aerospace Exploration Agency (JAXA), 2-1-1 Sengen, Tsukuba, Ibaraki 305-8505

¹⁴Department of Physics, Chuo University, 1-13-27 Kasuga, Bunkyo-ku, Tokyo 112-8551

¹⁵School of Dentistry at Matsudo, Nihon University, 2-870-1 Sakaecho-nishi, Matsudo, Chiba 101-8308

(Received (2011 July 25); accepted (2011 September 6))

Abstract

We report on the X-ray spectral analysis of the black hole candidate XTE J1752–223 in the 2009–2010 outburst, utilizing data obtained with the MAXI/Gas Slit Camera (GSC), the Swift/XRT, and Suzaku, which work complementarily. As already reported by Nakahira et al. (2010) MAXI monitored the source continuously throughout the entire outburst for about eight months. All the MAXI/GSC energy spectra in the high/soft state lasting for 2 months are well represented by a multi-color disk plus power-law model. The innermost disk temperature changed from ~ 0.7 keV to ~ 0.4 keV and the disk flux decreased by an order of magnitude. Nevertheless, the innermost radius is constant at $\sim 41 D_{3.5}(\cos i)^{-\frac{1}{2}}$ km, where $D_{3.5}$ is the source distance in units of 3.5 kpc and i the inclination. The multi-color disk parameters obtained with the MAXI/GSC are consistent with those with the Swift/XRT and Suzaku. The Suzaku data also suggests a possibility that the disk emission is slightly Comptonized, which could account for broad iron-K features reported previously. Assuming that the obtained innermost radius represents the innermost stable circular orbit for a non-rotating black hole, we estimate the mass of the black hole to be $5.51 \pm 0.28 M_{\odot} D_{3.5}(\cos i)^{-\frac{1}{2}}$, where the correction for the stress-free inner boundary condition and color hardening factor of 1.7 are taken into account. If the inclination is less than 49° as suggested from the radio monitoring of transient jets and the soft-to-hard transition in 2010 April occurred at 1–4% of Eddington luminosity, the fitting of the Suzaku spectra with a relativistic accretion-disk model derives constraints on the mass and the distance to be $3.1\text{--}55 M_{\odot}$ and $2.3\text{--}22$ kpc, respectively. This confirms that the compact object in XTE J1752–223 is a black hole.

Key words: accretion disks — black hole physics — stars: individual (XTE J1752–223) — X-rays: stars

1. Introduction

Galactic black hole candidates (BHCs) show various states characterized by their spectral shapes, temporal properties, and luminosities. They mostly take two major states, the “low/hard state” and the “high/soft state”, which are referred to as “the hard X-ray state” and “the thermal dominant state”, respectively, in more recent classification (see McClintock & Remillard 2006 and references therein) since the state of a BHC is not always determined by an X-ray luminosity alone. In the low/hard state, the X-ray energy spectra are dominated by a power-law component with a photon index of ~ 1.7 and a high energy cutoff at ~ 100 keV that shows strong short-time variability (Grove et al. 1998). They can be explained by thermal Comptonization of soft photons from the accretion disk by hot plasmas with a temperature of $\sim 10^{10}$ K (e.g., Makishima et al. 2008, Takahashi et al. 2008, Shidatsu et al. 2011a). In a typical outburst of a transient BHC, it generally exhibits a spectral transition from the low/hard to the high/soft state through the intermediate (or very high) state when the luminosity reaches $\sim 10\%$ of the Eddington limit. The X-ray spectra in the high/soft state are characterized by a ultra-soft component which is considered to originate from an optically-thick and geometrically-thin accretion disk (so called “standard disk”; Shakura & Sunyaev 1973). This emission can be successfully described by the multi-color disk (MCD) model (Mitsuda et al. 1984, Makishima et al. 1986) with the innermost temperature of ~ 1 keV. An important signature in the high/soft state is that the innermost radius (r_{in}) of the accretion disk is kept constant, independent of the flux or innermost disk temperature (e.g., Tanaka et al. 1996). Hence, it is believed that the r_{in} reflects the innermost stable circular orbit (ISCO), which is determined through general relativity by the mass and angular momentum of the black hole; the radius of ISCO for a non-spinning black hole is $6R_g$ ($R_g \equiv GM/c^2$ is the gravitational radius, where G , M , c are the gravitational constant, black hole mass, and light velocity, respectively). By assuming that the obtained innermost r_{in} to the ISCO, the black hole mass can be estimated from the X-ray spectrum alone for a given spin parameter.

XTE J1752–223 was first discovered with the Proportional Counter Array (PCA) onboard Rossi X-ray Timing Explorer (RXTE) on 2009 October 23 (MJD 55127) during a Galactic bulge scan observation (Markwardt et al. 2009). The Gas Slit Camera (GSC) onboard Monitor of All-sky X-ray Image (MAXI; Matsuoka et al. 2009) detected the source simultaneously (Nakahira et al. 2009). As described in Nakahira et al. (2010; hereafter Paper I), MAXI continuously monitored the source during the entire outburst until 2010 June. The MAXI light curves and hardness-intensity diagram revealed that the source initially stayed in the low/hard states with two stable flux levels for about three months, and then moved into the high/soft state (Paper I). A radio flare was detected simultaneously with the spectral transition (Negoro et al. 2010, Brocksopp et al. 2010), and the proper motion of the jet ejecta was later found with VLBI observations (Yang et al. 2010). Miller-Jones et al. (2011) identified it as an approaching jet ejected coincidentally with the X-ray state transition. From the observed flux of the approaching jet and its upper limit of the receding one, they constrained the jet speed and the inclination

angle from the line-of-sight to be $> 0.66c$ and $< 49^\circ$, respectively, by assuming that the axes of the twin jets are aligned. Shaposhnikov et al. (2010) estimated the black hole mass and distance to be $9.6 \pm 0.9 M_\odot$ and 3.5 ± 0.4 kpc, respectively, using the spectral-timing correlation technique (Shaposhnikov et al. 2009). However, the compact object mass has not been estimated via optical mass-function technique. To firmly establish the nature of XTE J1752–223, however, it is quite important to constrain the black hole mass by an independent approach.

In this paper, we present the results from a detailed spectral analysis of XTE J1752–223 utilizing the MAXI/GSC data, together with those of Swift/XRT and Suzaku, mainly focusing on the spectra in the high/soft state. We then discuss the constraints on the black hole mass and distance based on our results. In the appendix, we present the current status of spectral calibration of the MAXI/GSC using the Crab Nebula, which is fully reflected in this paper and in a similar work for the black hole candidate GX 339–4 reported by Shidatsu et al. (2011b). The spectral fitting was carried out on XSPEC version 12.6. Errors are quoted at statistical 90% confidence limits for a single parameter throughout the paper.

2. MAXI observation and analysis

2.1. MAXI observations

As the first astronomical mission on the International Space Station (ISS), MAXI has been operating since 2009 August. The payload carries two kinds of X-ray all-sky monitors; the Gas-Slit Camera (GSC; Mihara et al. 2011) and the Solid-state Slit Camera (SSC; Tsunemi et al. 2010, Tomida et al. 2011). The GSC consists of Xe-gas proportional counters for the X-ray detector and slat collimators with a slit to localize the direction of the incident X-rays. The counters employ resistive-carbon wires for detector anodes to determine the X-ray position along the anode wire. Twelve identical units (referred to as GSC_0, ..., GSC_9, GSC_A and GSC_B) are assembled so that they instantaneously cover two rectangular field of views (FoVs) of $3 \times 160 \text{ deg}^2$ with an equal area.

After the operation started in 2009 August, two counters, GSC_6 and GSC_9 were stopped on 2009 September 8 and 14, respectively, for high-voltage breakdown. Other two counters on GSC_A and GSC_B were stopped temporarily on September 23, because diagnostic data indicated that they may also break down rather soon. Consequently, the outburst of XTE J1752–223 from 2009 October to 2010 June was covered by eight GSC camera units out of the twelve.

The GSC FoV is limited by slats collimators. The visibility for a target at a given sky position changes according to the ISS orbital motion; hereafter we call the visibility time as “transit”. Each transit lasts for 40–150 s, and the effective area of each GSC counter change due to the triangular-shaped collimator transmission function, with a peak value of $4\text{--}5 \text{ cm}^2$. The MAXI/GSC scanned the direction of XTE J1752–223 2041 times in total from the discovery on 2009 October 23 (MJD 55127) to 2010 June 3 (MJD 55350). The total exposure times effective area becomes $534.8 \text{ cm}^2 \text{ ksec}$.

2.2. Analysis

For the data analysis, we used the MAXI specific analysis tools, which were developed by the MAXI team. We analyzed the GSC event data version 0.3b, which include the data taken by counters operated at the nominal high voltage (=1650 V) but excluding those of anode #1 and #2 whose energy responses have not been enough calibrated yet. We discarded events taken while the GSC FoVs were interfered by the solar panels and other ISS payloads. The events detected at the anode-end area were also screened since the background is higher therein. These event were cut with a condition that the photon incident angle (ϕ_{col} ; see Mihara et al. 2011 for the definition) is higher than 36° . As shown in Figure 1 we carefully extracted events for source and background from circular regions with a 1.5° radius, excluding regions within 1.7° of nearby sources, GX 5–1, GX 9+1 and SAX J1748.9–2021 in NGC 6440. We used only those data when the source and background regions were both fully scanned in a transit.

We performed spectral analysis of the data taken between MJD=55200 and MJD=55293, during which both the “hard-to-soft” and “soft-to-hard” transitions took place (Paper I). The net effective exposure was $194.5 \text{ cm}^2 \text{ ksec}$ for 752 transits. We divided the whole dataset into groups with typical lengths of a few days so that the spectrum in each group has enough photon statistics, except for the epoch around the “hard-to-soft” state transition when the spectrum changed rapidly. Eventually, data were separated into 49 groups whose exposures times effective area were $0.2 \sim 12 \text{ cm}^2 \text{ ksec}$. The energy response matrix for each group was calculated by the response builder (Sugizaki et al. 2011). The validity of the energy response was verified using the Crab Nebula (see Appendix).

2.3. Light Curves during the 2009–2010 Outburst

Figure 2 shows the MAXI/GSC light curves of XTE J1752–223 during the 2009–2010 outburst in the 2–4 keV, 4–10 keV, and 10–20 keV bands, together with the hardness ratio between the 4–10 keV and 2–4 keV bands. They are updated from those presented in Paper I, after applying the latest calibration and the same data screening as used for the spectral analysis (section 2.4 and Appendix). The MAXI/GSC first detected XTE J1752–223 at 15:05 (UT) on 2009 October 23 (MJD 55127) when the 2–20 keV X-ray intensity was 30 mCrab. It monitored the source almost uniformly except for the time when the FoV was close to the sun (MJD 55154–55159 and MJD 55172–55188) and when poles of the scanning axis was close to the source (around MJD 55300). The light curves reveal that the source stayed in the initial low/hard state for the extraordinary long period of about 3 months, and took two flux-plateau phases meantime (Paper I).

The “hard-to-soft” state transition occurred on MJD 55218 and the following behavior agrees well with those of the typical BHC outbursts (Remillard et al. 2006). The X-ray intensity was peaked at 420 mCrab on 2010 January 22 (MJD 55218), then decayed exponentially with an e-folding time of 34 days through the high/soft state. The “soft-to-hard” transition started on 2010 March 30 (MJD 55285), and then the source returned to the low/hard state on 2010 April 6 (MJD 55292). On 2010 June 28 (MJD 55375), the source flux fell be-

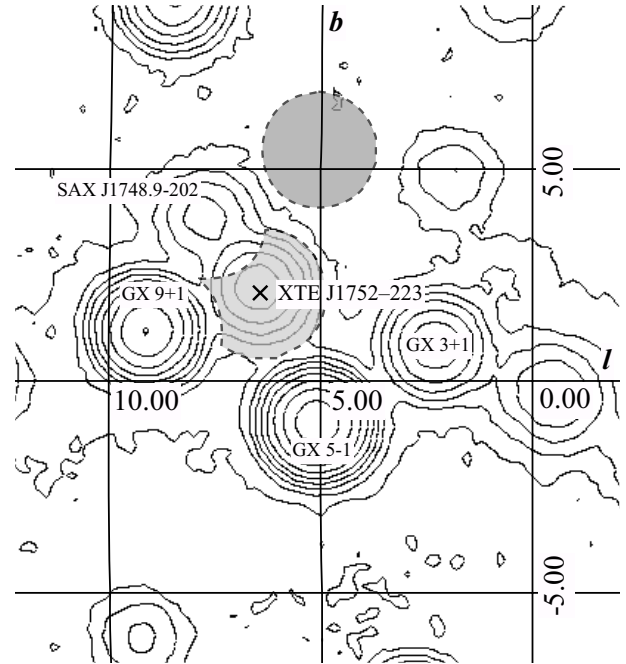


Fig. 1. A 2–20 keV MAXI/GSC image in the galactic coordinate around XTE J1752–223. The data are accumulated from MJD 55200 to MJD 55299. The intensity contours are shown by a log scale. The source and background regions for the analysis are indicated by the shadowed regions.

low the MAXI/GSC detection sensitivity per day (20 mCrab). Thus, the total duration of the outburst became about eight months.

2.4. Spectral Analysis

For the spectral analysis, we employed the standard model for BHCs in the high/soft state, a multi-color disk (MCD; *diskbb* in XSPEC) model plus a power-law representing the hard tail. The *wabs* (Morrison et al. 1983) model with solar abundances by Anders et al. (1982) was applied for the interstellar absorption. The hydrogen column density (N_{H}) toward XTE J1752–223 was fixed at $0.6 \times 10^{22} \text{ cm}^{-2}$, based on the Swift and Suzaku results as described below. The model has four parameters: the innermost temperature T_{in} and innermost radius r_{in}^1 for the MCD component, with the photon index Γ and normalization at 1 keV for the power-law component. We first applied the model to all the data. When the MCD component was found to be not necessary (i.e., the 90% confidence range of the MCD normalization contains zero), only the power-law model was applied with its Γ set free. When the MCD component was required, we fixed $\Gamma = 2.2$ for all the spectra because it is often difficult to determine from individual spectrum due to poor statistics and the limited energy coverage of the MAXI/GSC. This photon index corresponds to a typical value obtained when the power-law component is relatively strong (>50% of the total flux in the 2–20 keV band). Although Shaposhnikov et al. (2010) suggest from the

¹ $r_{\text{in}} = \sqrt{N_{\text{diskbb}}} (D/10 \text{ kpc}) (\cos i)^{-1/2}$, where N_{diskbb} is the normalization of the *diskbb* model. The distance to the source of $D = 3.5 \text{ kpc}$ and inclination angle $i=0$ are assumed.

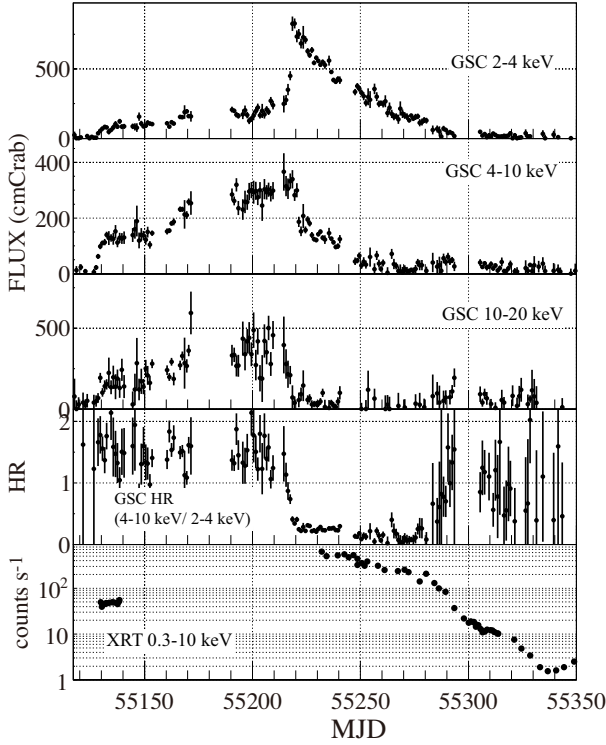


Fig. 2. MAXI/GSC and Swift/XRT light curves of XTE J1752-223 in the 2009-2010 outburst. Four panels from the top show the GSC light curves in three energy bands of 2–4, 4–10 and 10–20 keV, and the hardness ratio between the 4–10 keV and 2–4 keV bands. The bottom shows the Swift/XRT light curve in the 0.3–10 keV band.

RXTE/PCA data that the power-law slope is variable between $\Gamma \approx 1.6 - 2.2$ by using a spectral model different from ours, we confirmed that varying Γ value within this range only changes the best-fit MCD normalization by $< 3\%$, and hence does not affect our conclusions.

The MCD plus power-law model or single power-law model gave good fits for all the MAXI/GSC data. Table 1 summarizes the obtained spectral parameters, while figure 3 plots the evolution of the model parameters. Figure 4 shows typical response-unfolded νF_ν spectra, together with their best-fit models.

The spectra during MJD 55200–55214 (DataID = 1–10) required no MCD component. The photon indices and fluxes was almost constant meanwhile at ≈ 1.7 and $1.2 \times 10^{-8} \text{ erg cm}^{-2} \text{ s}^{-1}$, respectively. On MJD 55215.64–55216.15 (DataID = 11–12), the spectrum dramatically softened to $\Gamma \sim 2.0$. The MCD component then appeared after MJD 55216.65 (DataID = 13) and lasted until MJD 55286 (DataID = 46), although the power-law flux was dominant MJD 55216.65–55218.37 and on MJD 55286.97 in the 2–20 keV band. The MCD flux reached to a peak of $\sim 1 \times 10^{-8} \text{ erg s}^{-1} \text{ cm}^{-2}$ on 2010 January 23 (MJD 55219), and then decreased. The innermost temperature T_{in} gradually decreased from $\sim 0.7 \text{ keV}$ to $\sim 0.4 \text{ keV}$ toward MJD 55286.97. By contrast, the innermost radius r_{in} was almost constant at $\sim 41 \text{ km}$ (for $D = 3.5 \text{ kpc}$ and $i = 0^\circ$) then, except for the epoch before the state transition on MJD 55218.37 (DataID = 13–15).

Based on these results, we identify that the source was likely

in the low/hard state before MJD 55214, the intermediate state over MJD 55215–55218, the high/soft state over MJD 55219–55282, and then came back to the low/hard state after MJD 55292 through the intermediate state between MJD 55285 and 55292. For later discussions, we calculate the weighted average of r_{in} in the high/soft state to be $41.0 \pm 2.1 \text{ km}$, using the observations on MJD 55230–55282 when the contribution of the power-law component was sufficiently small.

As Steiner et al. (2009) pointed out the initial variation of r_{in} observed on MJD 55216–55218 in the intermediate state may be caused by the ignoring of Comptonized photons in the calculation of r_{in} . In these epochs, the fraction of the power-law component was $> 50\%$ of the total X-ray flux in the 2–20 keV band, and hence the Compton up-scattering of the disk blackbody emission can significantly reduce the normalization of the direct MCD component (McClintock & Remillard 2006). We find it difficult, however, to obtain a reliable estimate of the innermost radius corrected for this effect from the MAXI/GSC data alone, which strongly couples with the photon index of the Compton scattered component. We leave detailed investigation of the spectra in the intermediate state for future work, and concentrate on those in the high/soft state in the following analysis.

3. Swift Observations and Analysis

From 2009 October 25 to 2010 July 29, the Swift/XRT (Burrows et al. 2005) carried out 67 pointing observations of XTE J1752-223 in the Windowed Timing (WT) mode. Due to the Sun angle constraint, the observations were interrupted between 2009 November 4 (MJD 55139) and 2010 February 3 (MJD 55230). We analyzed data of 17 observations taken in the high/soft state after 2010 February 4 (MJD 55231). All the XRT spectra and light curves were produced by the web interface (Evans et al. 2009) supplied by the UK Swift Science Data Centre at the University of Leicester. We used the XRT response matrix file for the WT mode version 12. All the 17 observations with an exposure time of a few ksec each were analyzed independently.

First results of the Swift/XRT spectral analysis were already reported by Curran et al. (2010). They employed the same MCD plus power-law model as we used in the MAXI/GSC analyses, but derived a different result that the innermost radius changed significantly with time. The difference is considered to come from the fact that they left the power-law index free and obtained a wide range of Γ between ~ 0 and ~ 3 , even though this quantity is not constrained when the MCD component is strong. Hence we reanalyzed the XRT spectra by fixing Γ at 2.2, the same value as adopted for the MAXI/GSC spectra. The N_{H} was left free because the Swift/XRT is sensitive down to $\sim 0.3 \text{ keV}$. Resultant parameters are summarized in table 2, which are also plotted on figure 3. The values of r_{in} were thus constant, with at most 5% scatter around weighted mean of $r_{\text{in}} = 41.4 \pm 0.3 \text{ km}$.

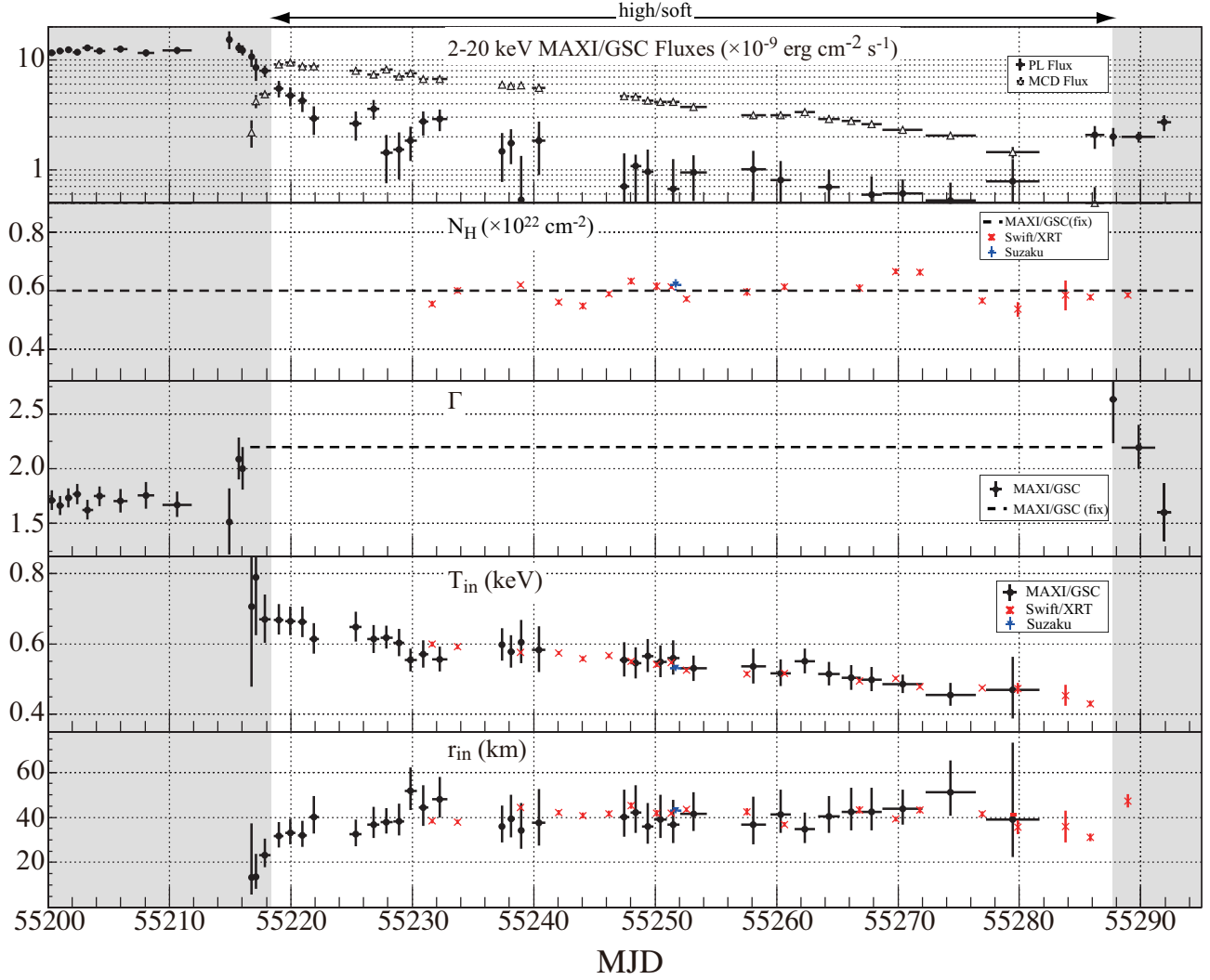


Fig. 3. Evolution of the spectral parameters of XTE J1752–223. The MAXI/GSC, Swift/XRT, and Suzaku results using the MCD plus power-law model are shown by black, red, and blue points, respectively. From top to bottom panels, 2–20 keV fluxes of MCD and power-law components, the hydrogen column density N_{H} , the photon index Γ , the innermost temperature T_{in} , and the innermost radius r_{in} are indicated.

4. Suzaku Observations and Results

4.1. Observation

We also observed XTE J1752–223 in the high/soft state with Suzaku (Mitsuda et al. 2007) as a Target-of-Opportunity (ToO) from 2010 February 24 (MJD 55251) 04:58:00 to February 25 04:27:24 (ObsID: 904005010). Suzaku carries 4 X-ray telescopes (XRT, Serlemitsos et al. 2007), each with a focal-plane X-ray CCD imager called XIS (X-ray Imaging Spectrometer; Koyama et al. 2007) covering the 0.2–12 keV energy band. Since XIS2 has not been available, the two remaining front-illuminated (FI) CCDs (XIS0 and XIS3) were operated for this observation together with the back-illuminated (BI) CCD (XIS1). The three XIS cameras were operated with burst and window options. The burst time, window size, and editing mode were “0.3 sec, 1/4 window, and 2×2 ” for XIS0 and XIS3, and “0.1 sec, normal window, and 3×3 ” for XIS1, respectively. The Hard X-ray Detector (HXD; Takahashi et al. 2007; Kokubun et al. 2007), covering the 10–70 keV energy

band with Si PIN photo-diodes (HXD-PIN), and the 50–600 keV range with GSO scintillation counters (HXD-GSO), was operated in the normal mode. The source was observed at the HXD nominal position.

4.2. Data Reduction

The data reduction and analyses were performed using Suzaku FTOOLS in HEASOFT version 6.10 provided by the NASA/GSFC Suzaku GOF. All the XIS and HXD data were reprocessed by the Suzaku pipeline processing version 2.4.12.27, with the latest calibration database (CALDBVER) hxd20090902, xis20090925, and xrt20080709.

The image degradation due to “thermal wobbling” of the satellite pointing was corrected by using the attitude file updated with AEATTCOR2. We screened the XIS data under the standard criteria, and discarded events during time intervals when the telemetry of the XIS was saturated. Resultant net exposure was 10.6 ksec and 449 sec for FIs and BI, respectively. The BI exposure was short, because 0.1 sec burst time

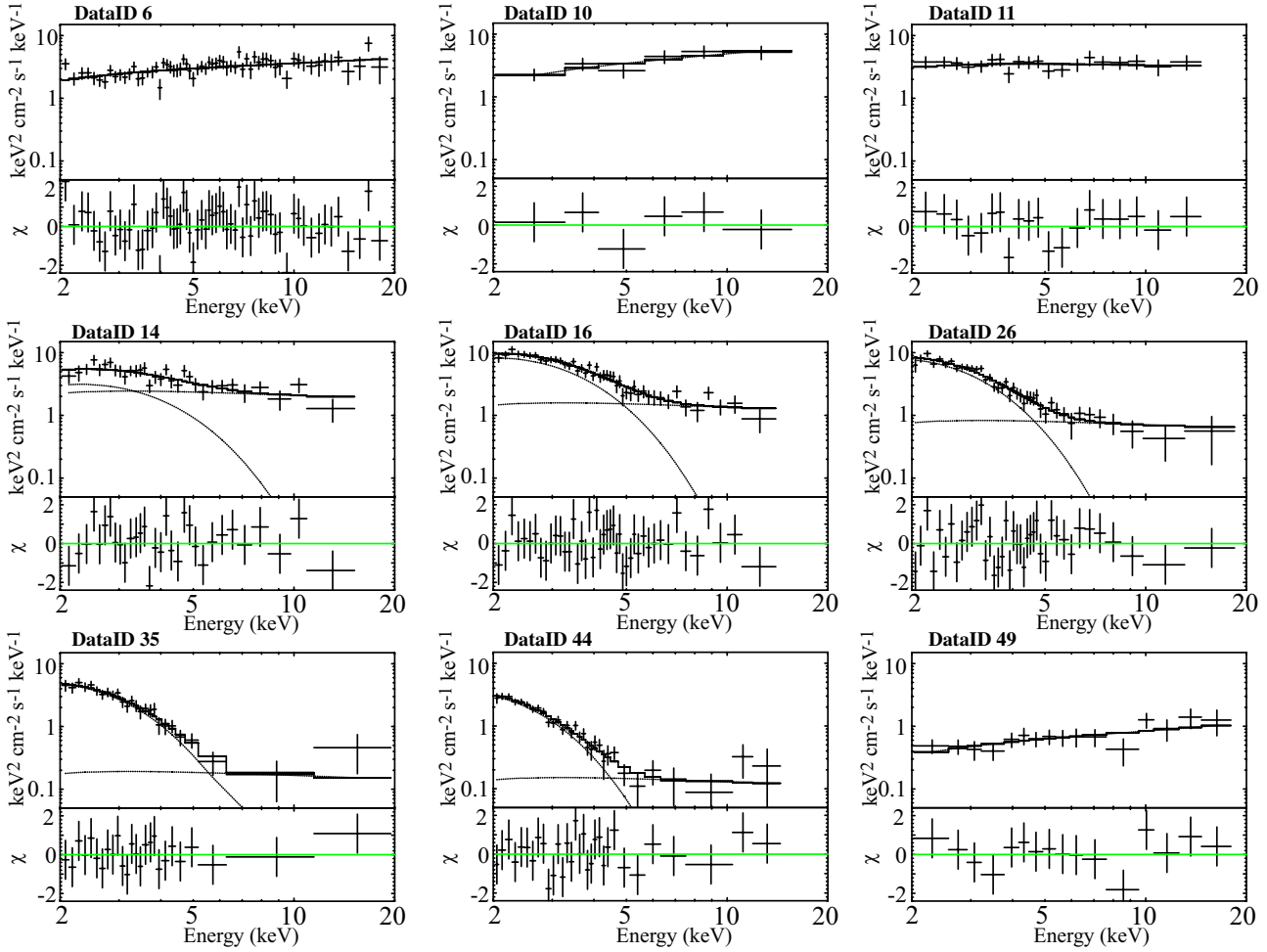


Fig. 4. Examples of the νF_ν spectrum of XTE J1752–223 observed with the MAXI/GSC together with the best-fit model. Panels correspond to DataIDs 6, 10, 11, 14, 16, 26, 35, 44, and 49. Data ID 35 was taken approximately at the same time as the Suzaku observation.

with normal window make the exposure 0.1 sec in 8 sec period and the exposure is one twelfth of each FI’s exposure. Furthermore, the fraction of out-of-time events (Koyama et al. 2007) is more significant in the BI data, which would introduce systematic uncertainties in the spectral analysis. Hence, we did not use the XIS1 data in this paper. The average 0.5–10 keV count rate was ~ 400 cts s^{-1} and ~ 700 cts s^{-1} with FIs and BI, respectively. We extracted the XIS0 and 3 events from a rectangle region of 8.6×4.5 tracing the 1/4 window area centered on the image peak, and the background from another region avoiding contaminating point sources. The source was so bright that the XIS suffered from photon pileup at the image center. Using the software of AEPILUPCHECKUP (Yamada et al. 2011 in preparation), which automatically detects the extent of pileup utilizing radial surface brightness profiles and other sets of information, we excluded a circular within 1/5 of the image peak for XIS0 and 3, to extract the events whose pileup fraction is below 1%. We combined the spectra and response files of the two FI cameras to increase the photon statistics in the spectra. To account for possible uncertainties in the instrument calibration (e.g. Makishima et al. 2008), systematic errors of 1% was assigned to each energy bin of the XIS spectra.

We obtained the cleaned HXD events with the standard criteria. After the dead-time correction, the net exposures of PIN and GSO were 21.2 and 27.0 ksec, respectively. The dead-time fraction was 18.2 and 7.5 % for PIN and GSO, respectively. The cosmic X-ray background (CXB) was modeled assuming an exponentially cutoff power-law model (Boldt 1987). The non-X-ray background (NXB) model is provided by the HXD team (Fukazawa et al. 2009). We used the model with METHOD=“LCFITDT(bgd_d)”, and the version of METHODV=“2.0ver0804” and “2.4ver0912-64” for the data of PIN and GSO, respectively. After subtracting the modeled NXB and CXB, the source signals were significantly detected by PIN up to 50 keV, above the systematic uncertainty on the NXB model ($\sim 3\%$). Since the GSO signals were comparable to the systematic errors of the NXB model there in ($\sim 1\%$), we consider the source detection with GSO insignificant.

4.3. Spectral Analysis

As shown in figure 5(a), we used an energy range of the 1.2–10 keV for the XIS spectrum and 15–50 keV for the HXD-PIN spectrum, where the calibrations of the energy responses were well established. The energy bands of 1.6–2.0 keV and 2.2–2.4 keV were excluded to avoid large systematic uncertainties of

the effective area near the Silicon K edge (1.74 keV and 1.84 keV for $K\alpha$ and $K\beta$, respectively) and gold M edge (2.29 keV), respectively. In the combined fit to the XIS and HXD-PIN spectra, we employed a cross normalization factor of 1.18 between XIS and PIN (SUZAKU-MEMO-2008-06).

We firstly fitted the spectra with the MCD plus power-law model modified by interstellar absorption (*wabs* model), the same one as adopted to fit the MAXI/GSC and Swift/XRT spectra in the previous sections. The residuals in units of χ are shown in the figure 5(b). The fit was found to be unacceptable ($\chi^2/dof = 230.1/136$), leaving an emission-line feature at ≈ 6.5 keV, and significant broad edge-like residuals above ~ 7 keV. These features may be explained away by several different approaches; e.g., by invoking a broad Fe-K line concept (Reis et al. 2010) or applying so-called smeared-edge model (e.g., Ebisawa et al. 1994; Dotani et al. 1998) to account for the edge structure. The latter approach with *wabs*smedge*(diskbb+powerlaw+gaus)* model gave an acceptable fit ($\chi^2/dof = 141.6/133$; fig 5(c)) with a maximum optical depth of $5.50^{+1.4}_{-0.75}$ for fixed edge energy and width of 7.11 keV and 10 keV, respectively. A narrow emission line was found at $E_c = 6.59^{+0.08}_{-0.07}$ keV with a 1σ line width of 10 eV (fixed) and an equivalent width of $EW = 63^{+42}_{-41}$ eV. These approaches are empirical and may be degenerate, however.

As an alternative possibility, we resorted to the idea of Kolehmainen et al. (2011) that the disk emission is broader than the simplest MCD model, which could lead to artificial detection of broad iron-K features. Assuming that weak Comptonization of the MCD emission took place, we replaced the *diskbb* model with a *compPS* model (Poutanen & Svensson 1996), which computes Compton scattering by hot corona using exact numerical solution radiative transfer equation. We chose “slab” (geom=1) geometry and a MCD spectrum as the seed photons. We left the optical depth of the corona τ as a free parameter but fixed the electron temperature at $T_e = 10$ keV and covering fraction at $\text{cov}_{\text{frac}} = 1$ to avoid strong coupling between these parameters; the choice of T_e did not affect our results on the disk parameters over the statistical errors. The presence of a fluorescence iron-K line at ≈ 6.6 keV indicates that a reflection continuum must be included in the model as well. Hence, we adopted *pexriv* model (Magdziarz & Zdziarski 1995) for the power-law component, which was considered to be the main source of irradiation onto the disk in the high/soft state. The model thus became *wabs*(compPS+pexriv+gaus)* in the XSPEC terminology. For the *pexriv* component, we assumed no high energy cutoff, and fixed the solid angle of the reflector at $\Omega = 2\pi$, inclination at 25° , and ionization parameter at $\xi_i = 1000 \text{ erg cm s}^{-1}$, which consistently explain both iron-K line intensity and center energy. The fit was found to be acceptable with $\chi^2/dof = 129.9/132$; as shown in the figure 5(d), the broad edge-like residuals mostly disappeared. The model gave an absorbed 2–20 keV flux of $(3.76 \pm 0.02) \times 10^{-9} \text{ erg s}^{-1} \text{ cm}^{-2}$. We obtained $\tau = 0.41 \pm 0.05$ and $\Gamma = 2.13 \pm 0.01$ in the *pexriv* component, a reasonable value in the high/soft state (e.g., Zdziarski et al. 2004). More detailed analysis, more advanced disk emission modeling, and relativistic Fe-K lines, is beyond the scope of this paper, and will be reported elsewhere.

The best-fit parameters of these models are listed in table 3. We note that by replacing the *diskbb* model with the *compPS* model, the best-fit value of r_{in} increased by 13%. This is because a spectrum hardened by Comptonization was assumed in the *compPS* model, an intrinsic temperature T_{in} became lower, leading to an increase in r_{in} . While the difference should be regarded as a systematic modeling uncertainty, we confirm that it does not affect our conclusion. The photon index of the hard tail ($\Gamma = 2.13 \pm 0.01$) is smaller than the result obtained from the same Suzaku data by Reis et al. (2010) ($\Gamma = 2.54^{+0.02}_{-0.11}$), who did not include the 15–20 keV and 45–50 keV bands in fitting the HXD/PIN spectrum.

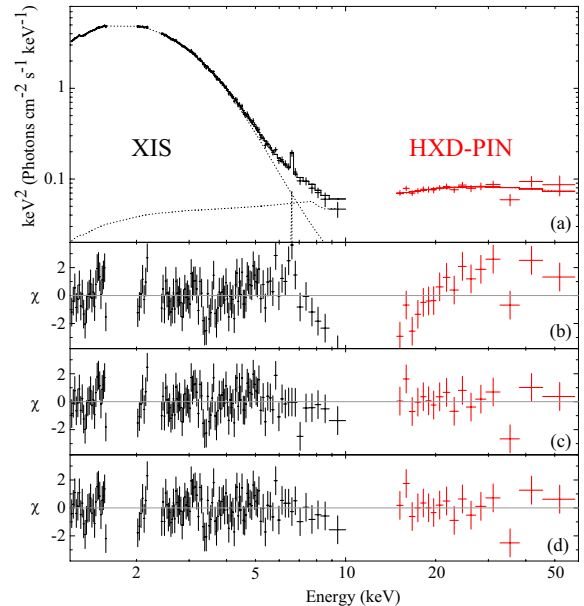


Fig. 5. (a) Suzaku response-unfolded $\nu F\nu$ spectrum of XTE J1752–223 from the best-fit for *wabs*(compPS+pexriv+gaus)*, and the residuals between the data and best-fit models for (b) *wabs*(diskbb+powerlaw)*, (c) *wabs*smedge*(diskbb+powerlaw+gaus)*, (d) *wabs*(compPS+pexriv+gaus)*.

5. Discussion

We have analyzed the MAXI/GSC, the Swift/XRT, and Suzaku data of XTE J1752–223 in the high/soft state from MJD 55218.62 to 55281.63. The overall continuum spectra were reproduced by the MCD plus power-law model with an interstellar absorption. The innermost temperature T_{in} decreased from ~ 0.7 keV to ~ 0.4 keV, while the innermost radius r_{in} remained constant. By assuming $D = 3.5$ kpc and $i = 0^\circ$, the values of r_{in} derived from the MAXI/GSC, Swift/XRT, and Suzaku data are 41.0 ± 2.1 km, 41.4 ± 0.3 km, and 42.9 ± 0.9 , respectively. The results from the three instruments are mutually consistent with each other within the statistical errors. For the following discussion, we employ 41.0 ± 2.1 km for r_{in} as determined from the MAXI/GSC, although we also discuss the case when the Suzaku result with the *compPS* model ($r_{\text{in}} = 47.2 \pm 0.8$ km) is adopted to take into account the possible systematic uncertainty.

Since the value of r_{in} thus estimated is significantly larger than those found in luminous low-mass X-ray binaries (10 km; Mitsuda et al. 1984), the black hole interpretation of XTE J1752–223 (Paper I; Muñoz-Darias et al. 2010) is considerably reinforced. Furthermore, its constancy allows us to identify it with the ISCO in the high/soft state. The stable r_{in} at 41.0 km is supposed to reach the ISCO in the high/soft state. We note that this r_{in} is an “apparent” innermost radius, and the “realistic” innermost radius (R_{in}) should be estimated as $R_{\text{in}} = \xi \kappa^2 r_{\text{in}}$ where the spectral hardening factor κ is 1.7 (Shimura & Takahara 1995) and correction factor for the boundary condition ξ is 0.412 (Kubota et al. 1998). The value of κ has been confirmed in recent work on disk models (e.g., Kubota et al. 2010; Done & Davis et al. 2008). When the central object is assumed to be a non-spinning black hole (i.e. Schwarzschild black hole), R_{in} should equal to $6R_g$. Then, the black-hole mass is estimated as

$$M = \frac{c^2 R_{\text{in}}}{6G} = 5.51 \pm 0.28 \left(\frac{D}{3.5 \text{ kpc}} \right) (\cos i)^{-\frac{1}{2}} M_{\odot}. \quad (1)$$

Using the inclination angle $i < 49^\circ$ obtained from radio observations (Miller-Jones et al. 2011), the black hole mass and distance are constrained in the shadowed area shown in figure 6. If we assume the distance to be 3.5 kpc, the mass will be $5.2\text{--}7.1 M_{\odot}$, and if $D=10$ kpc, $15.0\text{--}20.4 M_{\odot}$.

To validate our method to estimate the black hole mass by employing the MCD model which is a simplified approximation of a true disk spectrum, we also performed a spectral fit to the Suzaku spectra using the *kerrbb* model (Li et al. 2005). This model calculates the X-ray spectrum of a relativistic accretion disk around a rotating black hole by taking into account the innermost boundary condition and the effects of self-irradiation of the disk. Here we fixed the distance at $D=3.5$ kpc, spin parameter at $a=0$, and color correction factor at $\kappa=1.7$ for consistency with the previous discussion. The fit with the *wabs*(kerrbb+pexriv)* model was not acceptable ($\chi^2/\text{dof} = 215.5/135$), leaving similar residuals seen in figure 5(b). Thus, we employed the *simpl* model (Steiner et al. 2009) with a steep photon index fixed at 7.4 to approximately represent weak Comptonization of the disk emission; the model became *wabs*(simpl*kerrbb+pexriv+gaus)*, which was found to give an acceptable fit ($\chi^2/\text{dof} = 129.5/134$). The black hole mass derived for $i=0^\circ$ and $i=49^\circ$ is $4.98^{+0.28}_{-0.25} M_{\odot}$ and $8.43^{+0.44}_{-0.42} M_{\odot}$, respectively, which differs by $\sim 20\%$ from the mass presented in equation (1).

From past observations of BHCs and neutron stars Maccarone (2003) pointed out that the state transition from the high/soft state to the low/hard state occur at 1–4% (centered at 2%) of the Eddington luminosity². Judging from the change of the photon index, XTE J1752–223 went back to the low/hard state around MJD 55292 (DataID 49). The bolometric flux at the transition to be $F_{\text{trans}} = (6.68 \pm 0.83) \times 10^{-9} \text{ erg cm}^{-2} \text{ s}^{-1}$ assuming a cutoff power-law is continuum with $\Gamma = 1.8$ and a cutoff energy of 200 keV. Using the relation $0.01 < L_{\text{trans}}/L_{\text{edd}} < 0.04$ and $L_{\text{trans}} = 4\pi D^2 F_{\text{bol}}$, we can further constrain the distance and black hole mass of XTE J1752–223 as illustrated with the hatched region in fig-

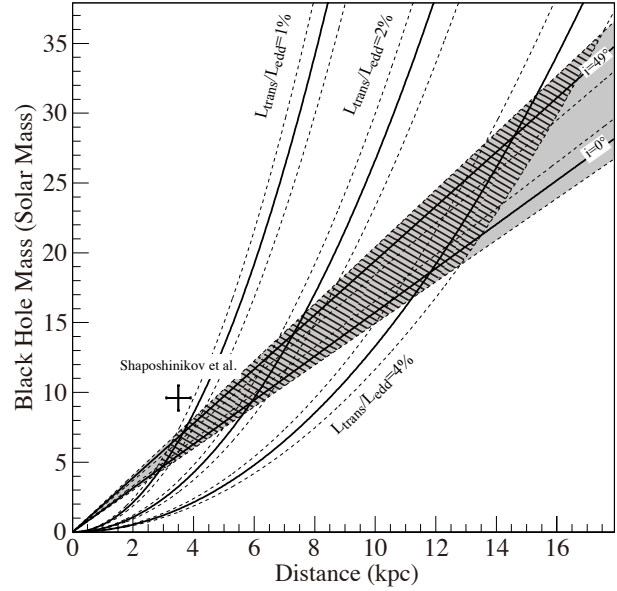


Fig. 6. Observational constraints on the mass and distance of XTE J1752–223. The shadowed region is specified by the innermost radius derived from the MAXI/GSC spectra in combination with the inclination angle $i < 49^\circ$ from the radio observation (Miller-Jones et al. 2011). Each solid line with two dashed lines indicates the best fit parameter and 90% confidence ranges of flux and r_{in} . The hatched region is derived assuming the empirical relation that the soft-to-hard transition occurs at $1\sim 4\%$ L_{edd} .

ure 6. Thus we can obtain $D=2.5\text{--}18$ kpc and $M=3.7\text{--}36 M_{\odot}$. When we instead use the Suzaku results, $D=3.0\text{--}20$ kpc and $M=5.3\text{--}44 M_{\odot}$ (based on the *wabs*(compPS+pexriv+gaus)* model) or $D=2.3\text{--}22$ kpc and $M=3.1\text{--}55 M_{\odot}$ (based on the *wabs*(simpl*kerrbb+pexriv+gaus)*) are derived.

Since we obtain $M > 3M_{\odot}$, our method of estimating M assuming a black hole is self consistent. The conclusion that the compact object in XTE J1752–223 is a black hole is robust against the assumptions that the rotational axis of the accretion disk and jet axis is exactly aligned and that the black hole is non-spinning, since the extreme conditions $i = 0^\circ$ and $a=0$ yield the smallest mass estimate. The values of $M=9.6 \pm 0.9 M_{\odot}$ and $D=3.5 \pm 0.4$ kpc estimated by Shaposhnikov et al. (2010) are outside the hatched region. If the black hole in XTE J1752–223 is spinning and/or the disk has a larger inclination than 49° , then the discrepancy could be solved.

6. Conclusions

Using data obtained by the MAXI/GSC, the Swift/XRT, and Suzaku, we have performed X-ray spectral analysis of the black hole candidate XTE J1752–223 in the high/soft state. As commonly seen in BHCs, the innermost radius remained constant in this state during the continuous observation with the MAXI/GSC. The results using the MCD plus power-law model were consistent between the three observatories. Detailed spectral modeling using Suzaku data suggests a possibility that the MCD emission may be slightly Comptonized, which could explain apparently broad iron-K features. Assuming that the innermost radius of the disk corresponds to the ISCO

² $L_{\text{edd}} = 1.5 \times 10^{38} \frac{M}{M_{\odot}} \text{ erg s}^{-1}$ for the solar abundances

and the black hole is non-spinning, we estimated the mass of the central object as $5.51 \pm 0.28 M_{\odot} \left(\frac{D}{3.5 \text{ kpc}} \right) (\cos i)^{-\frac{1}{2}}$ with corrections for the stress-free inner boundary condition and color hardening factor of 1.7. Furthermore, using the observational results that the inclination angle i is smaller than 49° from radio observations and the “soft-to-hard” transition occurs at 1–4 % Eddington luminosity, the distance and black hole mass of XTE J1752–223 were constrained as 3.1–55 M_{\odot} and 2.3–22 kpc, respectively, based on an analysis of the Suzaku spectra with a relativistic accretion disk model. Thus we can conclude that XTE J1752–223 is likely a black hole.

This research has made use of MAXI data provided by RIKEN, JAXA and the MAXI team. Suzaku data is provided by a collaborative mission between the space agencies of Japan (JAXA) and the USA (NASA). We also thank the Swift team for their observation. This work made use of data supplied by the UK Swift Science Data Centre at the University of Leicester. This research was partially supported by the Ministry of Education, Culture, Sports, Science and Technology (MEXT), Grant-in-Aid No.19047001, 20041008, 20540230, 20244015, 20540237, 21340043, 21740140, 22740120. One of the authors (S. N.) is grateful to a grant from the Hayakawa Satio Fund awarded by the Astronomical Society of Japan.

References

- Anders, E., & Ebihara, M., 1982, *Geochimica et Cosmochimica Acta* 46, 2363
- Brocksopp, C., et al., 2010, *The Astronomer’s Telegram* #2400
- Boldt, E., et al., *Phys. Rep.*, 1987, 146, 215
- Burrows, D. N., et al. 2005., *Space Sci. Rev.* 120, 165
- Curran, P. A., et al., 2011, *MNRAS*, 410, 1, 541
- Done, C., & Davis, S. W., 2008, *ApJ*, 683, 389
- Dotani, T., et al., 1997, *ApJ*, 485, L87
- Ebisawa, K., et al., 1994, *PASJ*, 46, 375
- Evans, P. A., et al., 2009, *MNRAS*, 397, 1177
- Fukazawa, Y., et al., 2009, *PASJ*, 61, S17
- Grove, J. E., and Strickman, M. S., 1998, *ApJ*, 502, L45
- Kirsch, M. G., et al. 2005, *Proc. SPIE*, 5898, 22
- Koyama, K., et al., 2007, *PASJ*, 59, S23
- Kolehmainen, M., et al., 2011, *MNRAS*, 416, 311
- Kokubun, M., et al., 2007, *PASJ*, 59, S53
- Kubota, A., et al., 1998, *PASJ*, 50, 667
- Kubota, A., et al., 2010, *ApJ*, 714, 860
- Li, L.-X., Zimmerman, E. R., Narayan, R., & McClintock, J. E., 2005, *ApJS*, 157, 335
- McClintock, J. E., Remillard, R. E., et al., 2009, *ApJ*, 698, 1398
- Maccarone, T. J., 2003, *A&A*, 409, 697
- Morrison, R., & McCammon, D., 1983, *ApJ*, 270, 11
- Magdziarz, P., & Zdziarski, A. A., 1995, *MNRAS*, 273, 837
- Makishima, K., et al., 1986, *ApJ*, 308, 635
- Makishima, K., et al., 2008, *PASJ*, 60, 585
- Markwardt, C. B., et al., 2009, *The Astronomer’s Telegram* #2258.
- Matsuoka, M., et al., 2009, *PASJ*, 61, 999
- Mihara, T., Nakajima, M., Sugizaki, M., et al., 2011, *PASJ*, in print, arXiv:1103.4224
- Miller-Jones, J. C. A., et al., 2011, *MNRAS*, 415, 306
- Mitsuda, K., et al., 1984, *PASJ*, 36, 741
- Mitsuda, K., et al., 2007, *PASJ*, 59 S1
- Morii, M., Sugimori, K., & Kawai, N., 2011, *Physica E: Low-dimensional Systems and Nanostructures*, 43, 692
- Muñoz-Darias, T., et al., 2010, *MNRAS*, 404, L94
- Nakahira, S., et al., 2009, *The Astronomer’s Telegram* #2259
- Nakahira, S., et al. 2010, *PASJ*, 62, L28
- Negoro, H., et al., 2010, *The Astronomer’s Telegram* # 2396
- Poutanen, J. & Svensson, R., 1996, *ApJ*, 470, 249
- Reis, R. C, et al., 2010, *MNRAS*, 410, 2497
- Remillard, R. E. & McClintock, J. E., 2006, *ARA&A*, 44, 49
- Serlemitsos, P. J., et al., 2007, *PASJ*, 59, S9
- Shakura, N. I., & Sunyaev, R. A. 1973, *A&A*, 24, 337
- Shaposhnikov, N., and Titarchuk, L., *ApJ*, 2009, 699, 453
- Shaposhnikov, N, et al., 2010., *ApJ*, 723, 1817
- Shidatsu, M., et al., 2011a, *PASJ*, in print, arXiv:1105.3586
- Shidatsu, M., et al., 2011b, *PASJ*, submitted in this issue
- Shimura, T., & Takahara, F., 1995, *ApJ*, 445, 780
- Steiner, J. F., Narayan, R., McClintock, J. E., Ebisawa, K., 2009, *PASP*, 121, 1279
- Sugizaki, M., Mihara, T., et al., 2011, *PASJ*, in print, arXiv:1102.0891
- Takahashi, H., et al., 2008, *PASJ*, 60, S69
- Takahashi, T., et al., 2007, *PASJ*, 59, S35
- Tanaka, Y., & Shibazaki, N., 1996, *ARA&A*, 34, 607
- Tomida, H., et al., 2011, *PASJ*, in print.
- Toor, A., & Seward, F.D., 1974, *AJ*, 79, 995
- Tsunemi, H., et al., 2010, *PASJ*, 62, 1371
- Wilson-Hodge, C. A., et al. 2011, *ApJ*, 727, L40
- Yamada, S., et al. 2011 in preparation
- Yang, J., Brocksopp, C et al. 2010, *MNRAS*, L64
- Zdziarski, A. A., & Gierliński, M., 2004, *Prog. Theor. Phys. Suppl.* 155, 9

Table 1. Best fit parameters of MAXI observations.

DataID	MJD start–end	exposure (cm ² ksec)	Γ	power-law flux*	T_{in} (keV)	r_{in} (km)	Disk flux*	χ^2_{ν}/dof
1	55200.03–55200.66	3.42	1.71 \pm 0.09	11.6 \pm 0.7	–	–	–	1.33(59)
2	55200.73–55201.30	3.41	1.67 \pm 0.09	12.1 \pm 0.7	–	–	–	1.36(61)
3	55201.42–55202.00	3.42	1.73 \pm 0.09	12.4 \pm 0.7	–	–	–	0.92(64)
4	55202.06–55202.76	3.41	1.77 \pm 0.09	11.8 \pm 0.7	–	–	–	0.79(60)
5	55202.82–55203.71	3.41	1.63 \pm 0.09	13.0 \pm 0.7	–	–	–	0.81(65)
6	55203.77–55204.72	3.40	1.75 \pm 0.09	12.1 \pm 0.7	–	–	–	0.93(62)
7	55205.42–55206.56	2.37	1.70 \pm 0.11	12.6 \pm 0.8	–	–	–	1.10(47)
8	55207.38–55208.73	2.01	1.76 $^{+0.13}_{-0.12}$	11.6 \pm 0.9	–	–	–	0.57(36)
9	55209.41–55211.84	2.01	1.67 $^{+0.12}_{-0.11}$	12.2 \pm 0.9	–	–	–	1.13(39)
10	55214.88–55214.94	0.24	1.51 $^{+0.31}_{-0.30}$	15.4 $^{+2.9}_{-2.8}$	–	–	–	0.67(4)
11	55215.64–55215.83	0.83	2.09 \pm 0.19	13.0 \pm 1.3	–	–	–	0.55(18)
12	55215.89–55216.15	0.83	2.00 $^{+0.20}_{-0.19}$	12.3 $^{+1.4}_{-1.3}$	–	–	–	0.87(17)
13	55216.65–55216.91	1.06	2.20(fix)	10.7 $^{+1.7}_{-2.0}$	0.71 $^{+0.29}_{-0.23}$	13.3 $^{+23.9}_{-7.6}$	2.2 \pm 0.6	1.09(24)
14	55216.97–55217.29	1.28	2.20(fix)	8.5 $^{+1.8}_{-2.1}$	0.79 $^{+0.19}_{-0.16}$	13.5 $^{+10.4}_{-5.2}$	4.2 \pm 0.6	0.94(29)
15	55217.42–55218.37	3.39	2.20(fix)	8.0 $^{+0.9}_{-1.0}$	0.67 \pm 0.07	23.2 $^{+7.4}_{-5.3}$	4.9 \pm 0.4	0.86(51)
16	55218.62–55219.38	2.93	2.20(fix)	5.5 \pm 1.0	0.67 $^{0.05}_{-0.04}$	31.8 $^{+6.3}_{-5.0}$	9.2 \pm 0.5	0.73(42)
17	55219.57–55220.39	3.22	2.20(fix)	4.7 \pm 0.9	0.66 \pm 0.04	33.1 $^{+6.2}_{-5.0}$	9.6 $^{+0.5}_{-0.4}$	0.77(43)
18	55220.58–55221.35	3.06	2.20(fix)	4.3 \pm 0.9	0.66 \pm 0.04	32.0 $^{+6.4}_{-5.1}$	8.7 \pm 0.4	0.63(40)
19	55221.54–55222.30	2.27	2.20(fix)	3.0 $^{+0.8}_{-0.9}$	0.61 \pm 0.04	40.1 $^{+9.3}_{-7.2}$	8.8 \pm 0.5	1.11(33)
20	55224.84–55225.85	3.03	2.20(fix)	2.6 \pm 0.8	0.65 \pm 0.04	32.5 $^{+6.6}_{-5.2}$	8.0 \pm 0.4	1.15(35)
21	55226.30–55227.31	3.31	2.20(fix)	3.6 \pm 0.7	0.61 \pm 0.04	36.9 $^{+7.7}_{-6.2}$	7.4 \pm 0.4	0.63(39)
22	55227.37–55228.39	3.53	2.20(fix)	1.4 \pm 0.7	0.62 \pm 0.03	38.0 $^{+6.2}_{-5.2}$	8.2 \pm 0.4	1.13(33)
23	55228.45–55229.34	3.33	2.20(fix)	1.5 \pm 0.7	0.60 \pm 0.04	38.2 $^{+7.9}_{-6.2}$	7.1 \pm 0.4	1.19(30)
24	55229.41–55230.36	3.82	2.20(fix)	1.8 \pm 0.6	0.55 \pm 0.03	51.7 $^{+10.5}_{-8.4}$	7.6 \pm 0.3	1.25(32)
25	55230.55–55231.31	3.40	2.20(fix)	2.7 \pm 0.7	0.57 \pm 0.04	44.3 $^{+10.1}_{-8.0}$	6.7 \pm 0.4	1.29(34)
26	55231.63–55232.90	4.30	2.20(fix)	2.9 $^{+0.6}_{-0.7}$	0.56 $^{+0.04}_{-0.03}$	48.0 $^{+10.1}_{-8.1}$	6.8 \pm 0.3	0.93(38)
27	55237.15–55237.62	2.66	2.20(fix)	1.5 \pm 0.7	0.60 \pm 0.05	36.0 $^{+9.3}_{-7.1}$	6.0 \pm 0.4	0.79(26)
28	55237.87–55238.45	2.84	2.20(fix)	1.7 \pm 0.6	0.58 \pm 0.05	39.3 $^{+10.8}_{-8.1}$	5.8 \pm 0.4	0.96(27)
29	55238.82–55239.14	1.56	2.20(fix)	0.5 $^{+0.8}_{-0.5}$	0.61 \pm 0.06	34.3 $^{+12.1}_{-8.4}$	5.9 \pm 0.5	1.32(18)
30	55239.84–55240.99	1.60	2.20(fix)	1.8 \pm 0.9	0.58 $^{0.07}_{-0.06}$	37.5 $^{+15.0}_{-10.0}$	5.6 \pm 0.5	1.16(20)
31	55247.06–55247.89	3.22	2.20(fix)	0.7 \pm 0.7	0.55 \pm 0.05	40.2 $^{12.0}_{-8.9}$	4.7 \pm 0.3	0.73(23)
32	55247.95–55248.84	3.24	2.20(fix)	1.1 $^{+0.3}_{-0.6}$	0.55 $^{+0.05}_{-0.04}$	42.1 $^{+12.1}_{-9.0}$	4.6 \pm 0.3	0.61(24)
33	55248.91–55249.86	3.17	2.20(fix)	1.0 \pm 0.6	0.57 \pm 0.05	36.0 $^{+10.4}_{-7.7}$	4.2 \pm 0.3	0.92(24)
34	55249.92–55250.94	3.32	2.20(fix)	0.5 \pm 0.5	0.55 $^{+0.05}_{-0.04}$	39.1 $^{+11.1}_{-8.3}$	4.2 \pm 0.3	0.96(21)
35	55251.00–55252.02	3.22	2.20(fix)	0.7 \pm 0.6	0.56 \pm 0.05	36.7 $^{+11.0}_{-8.0}$	4.2 \pm 0.3	0.41(23)
36	55252.08–55254.24	5.51	2.20(fix)	0.9 \pm 0.4	0.53 $^{+0.04}_{-0.03}$	41.6 $^{+9.7}_{-7.6}$	3.7 \pm 0.2	0.84(28)
37	55257.09–55259.12	3.83	2.20(fix)	1.0 \pm 0.5	0.54 \pm 0.05	36.9 $^{+12.5}_{-8.9}$	3.1 \pm 0.2	0.66(23)
38	55259.52–55261.16	6.53	2.20(fix)	0.8 \pm 0.4	0.52 \pm 0.04	41.4 $^{+10.8}_{-8.2}$	3.1 \pm 0.2	0.53(26)
39	55261.49–55263.19	6.82	2.20(fix)	0.3 \pm 0.3	0.55 $^{+0.04}_{-0.03}$	34.7 $^{+7.6}_{-6.0}$	3.3 \pm 0.2	0.99(27)
40	55263.44–55265.22	8.85	2.20(fix)	0.7 \pm 0.3	0.51 \pm 0.03	40.4 $^{+9.0}_{-7.1}$	2.9 \pm 0.1	0.54(29)
41	55265.35–55266.94	8.52	2.20(fix)	0.4 \pm 0.3	0.50 $^{+0.04}_{-0.03}$	42.4 $^{+10.6}_{-8.1}$	2.8 \pm 0.1	1.11(25)
42	55267.00–55268.66	8.37	2.20(fix)	0.6 \pm 0.3	0.50 $^{+0.04}_{-0.03}$	42.4 $^{+10.6}_{-8.2}$	2.6 \pm 0.1	0.94(27)
43	55268.72–55272.02	16.93	2.20(fix)	0.6 \pm 0.2	0.49 \pm 0.03	43.7 $^{+8.5}_{-6.9}$	2.3 \pm 0.1	0.94(36)
44	55272.28–55276.41	12.51	2.20(fix)	0.5 \pm 0.2	0.46 \pm 0.03	51.3 $^{+13.9}_{-10.5}$	2.0 \pm 0.1	0.72(29)
45	55277.23–55281.63	3.98	2.20(fix)	0.8 \pm 0.5	0.47 $^{+0.09}_{-0.08}$	39.0 $^{+34.2}_{-16.6}$	1.4 \pm 0.2	0.94(14)
46	55285.44–55286.97	2.34	2.20(fix)	2.1 $^{+0.4}_{-0.5}$	0.31 $^{+0.20}_{-0.14}$	118.7 $^{+2179.5}_{-111.7}$	0.5 \pm 0.2	0.46(9)
47	55287.41–55288.05	2.42	2.63 $^{+0.47}_{-0.40}$	2.0 \pm 0.4	–	–	–	0.39(9)
48	55288.43–55291.16	8.98	2.19 $^{+0.21}_{-0.19}$	2.0 \pm 0.2	–	–	–	0.58(32)
49	55291.35–55292.49	3.41	1.60 $^{+0.27}_{-0.26}$	2.7 $^{+0.5}_{-0.4}$	–	–	–	0.61(14)

Note.

* In unit of 10^{-9} erg s $^{-1}$ cm $^{-2}$ (2–20 keV).

Table 2. Best-fit parameters of Swift/XRT observations.

ObsID	MJD start	Exposure (sec)	N_H ($\times 10^{22} \text{ cm}^{-2}$)	power-law flux*	T_{in} (keV)	r_{in} (km)	Disk flux*	χ^2_{ν}/dof
00031532010	55231.6	1374.3	0.56 ± 0.01	2.34 ± 0.23	0.60 ± 0.01	$38.4^{+1.1}_{-1.0}$	5.66 ± 0.20	1.68(224)
00031532011	55233.7	1595.0	0.60 ± 0.01	2.40 ± 0.19	0.59 ± 0.01	38.0 ± 1.0	5.39 ± 0.14	1.29(238)
00031532012	55238.9	2360.7	0.62 ± 0.01	1.26 ± 0.11	0.58 ± 0.01	$44.3^{+0.8}_{-0.7}$	6.39 ± 0.11	1.50(244)
00031532014	55242.0	1421.4	0.56 ± 0.01	2.41 ± 0.19	0.57 ± 0.01	42.2 ± 1.1	5.21 ± 0.15	1.64(234)
00031532015	55244.0	1123.8	0.55 ± 0.01	1.07 ± 0.17	0.56 ± 0.01	$40.9^{+1.3}_{-1.2}$	$4.31^{+0.17}_{-0.16}$	1.22(191)
00031532016	55246.2	1411.8	0.59 ± 0.01	2.80 ± 0.18	0.57 ± 0.01	41.7 ± 1.1	$4.79^{+0.13}_{-0.12}$	1.56(241)
00031532018	55248.0	835.6	0.63 ± 0.01	1.29 ± 0.16	0.55 ± 0.01	45.3 ± 1.4	$5.01^{+0.14}_{-0.13}$	0.95(202)
00031532019	55250.1	1144.3	0.61 ± 0.01	0.47 ± 0.12	0.54 ± 0.01	41.7 ± 1.4	$3.96^{+0.16}_{-0.14}$	1.22(177)
00031532020	55251.3	3026.5	0.61 ± 0.01	0.87 ± 0.07	0.55 ± 0.01	41.9 ± 0.7	4.07 ± 0.07	1.62(238)
00031532021	55252.6	1524.0	0.57 ± 0.01	0.65 ± 0.09	0.53 ± 0.01	43.4 ± 1.1	3.80 ± 0.06	1.50(193)
00031640001	55257.6	890.9	0.60 ± 0.01	0.69 ± 0.11	0.52 ± 0.01	$42.5^{+1.6}_{-1.5}$	3.05 ± 0.08	1.22(174)
00031640002	55260.7	909.9	0.61 ± 0.01	0.25 ± 0.05	0.52 ± 0.01	$36.9^{+1.1}_{-1.0}$	$2.23^{+0.09}_{-0.08}$	1.34(180)
00031640003	55266.8	1209.8	0.61 ± 0.01	0.17 ± 0.06	0.50 ± 0.01	$43.4^{+1.5}_{-1.4}$	2.38 ± 0.09	1.25(161)
00031640004	55269.8	1184.1	0.67 ± 0.01	0.32 ± 0.04	0.50 ± 0.01	$39.3^{+1.0}_{-0.9}$	2.00 ± 0.05	1.61(197)
00031640005	55271.8	1214.6	0.66 ± 0.01	0.33 ± 0.04	0.48 ± 0.01	43.3 ± 1.3	1.75 ± 0.06	1.41(181)
00031640006	55276.9	977.8	0.57 ± 0.01	0.34 ± 0.04	0.48 ± 0.01	$41.5^{+1.2}_{-1.1}$	1.67 ± 0.04	1.34(177)
00031640007	55279.8	128.3	$0.54^{+0.03}_{-0.02}$	± 0.12	0.47 ± 0.01	$35.8^{+3.1}_{-2.8}$	$0.99^{+0.11}_{-0.10}$	1.00(108)

Notes.

Photon indices was fixed to 2.20.

* In unit of $10^{-9} \text{ erg s}^{-1} \text{ cm}^{-2}$ (2–20 keV).**Table 3.** Best-fit parameters for the Suzaku observation.

Model					
<i>wabs</i>	<i>diskbb</i> / <i>compPS</i> [†]	<i>powerlaw</i> / <i>pexriv</i>	<i>gaus</i> ^{**}	<i>smedge</i> ^{††}	
N_H^*	T_{in} (keV)	Γ	E_c (keV)	$\tau_{\text{max}}^{\ddagger\ddagger}$	$\chi^2 / \text{d.o.f.}$
	r_{in}^{\ddagger} (km)	norm [#]	EW (eV)		
	τ^{\S}				
<i>wabs*(diskbb+powerlaw)</i>					
0.62 ± 0.02	0.53 ± 0.01	2.29 ± 0.06	230.1/136
...	42.9 ± 0.9	0.16 ± 0.03
...
<i>wabs*smedge*(diskbb+powerlaw+gaus)</i>					
0.65 ± 0.02	0.526 ± 0.003	2.22 ± 0.05	$6.59^{+0.08}_{-0.07}$	$5.50^{+1.4}_{-0.75}$	141.80/133
...	44.0 ± 1.0	0.16 ± 0.02	63^{+42}_{-41}
...
<i>wabs*(compPS+pexriv+gaus)</i>					
0.67 ± 0.02	$0.507^{+0.005}_{-0.006}$	2.13 ± 0.01	$6.60^{+0.08}_{-0.07}$...	131.4/133
...	47.2 ± 0.8	$0.05^{+0.08}_{-0.04}$	98 ± 43
...	0.41 ± 0.05

Notes.

* In unit of 10^{22} cm^{-2} .[†] T_e and cov_{frac} are fixed at 10 keV and at 1, respectively. No reflection from the *compPS* component itself is considered.[‡] $D=3.5 \text{ kpc}$ and $i=0^\circ$ are assumed.[§] Optical depth of the corona.^{||} Fixed at $\Omega = 2\pi$, $i = 25^\circ$ and $\xi_i = 1000 \text{ erg cm/s}$. No high energy cutoff is set in the incident power law continuum.[#] A normalization in unit of photons $\text{cm}^{-2} \text{ s}^{-1}$ at 1 keV.* 1 σ line width is fixed at 10 eV.^{††} The edge energy and width, photo-electric cross-section are fixed at 7.11 keV, 10 keV and -2.67, respectively.^{‡‡} The maximum absorption factor at threshold.

Appendix 1. MAXI/GSC spectral calibration using the Crab Nebula

We here show the status of the GSC energy response calibration with Crab-nebula data to confirm the validity of the spectral analysis. We used event data with the process version 0.3b, which is screened with the operation high voltage of a nominal 1650 V and the anode number of #0, #3, #4, and #5 whose positional response had been well established. The event selection is same as that employed in the first performance verification in Sugizaki et al. (2011).

We here screened the event data with more severe conditions to verify the response calibration with a better accuracy. We selected events taken only during such a good scan transit that the source incident angle ϕ_{col} is $< 36^\circ$ and the area for both the source and the background are completely covered.

The calibration of the energy response was performed using the screened background and Crab Nebula data in the following steps; The energy-PHA relations, which depend on the detector position along the anode wires, are corrected by a gain factor for each output amplifier. The parameter was calibrated using fluorescent lines in the background spectrum from Ti (4.51 keV) and Cu (8.04 keV) as well as the calibration source ^{55}Fe (5.895 keV). We verified that the gain factor obtained with a 0.1 % precision successfully reproduce gain position dependence within the discrepancy of 1% in RMS throughout the whole detector area. The threshold and the resolution of the Lower-Discriminator (LD) of each amplifier were then calibrated using the Crab Nebula spectra. The LD parameters were tuned so that the results of the spectral fit to an absorbed power-law model agrees with those of the canonical values, photon index $\Gamma = 2.1$ and hydrogen absorption column density $N_{\text{H}} = 0.35 \times 10^{22} \text{ cm}^{-2}$ (i.e. Toor & Seward 1974, Kirsch et al. 2005).

Figure A-1 shows the best-fit parameters to GSC Crab Nebula spectra. The data of multiple scan transits whose total exposure of $> 3.2 \text{ cm}^2 \text{ ksec}$ were grouped so that each spectrum has enough photon statistics to constrain parameters of a power-law model. Table A-1 summarizes the results. The derived parameters agree with the canonical values within the statistical errors.

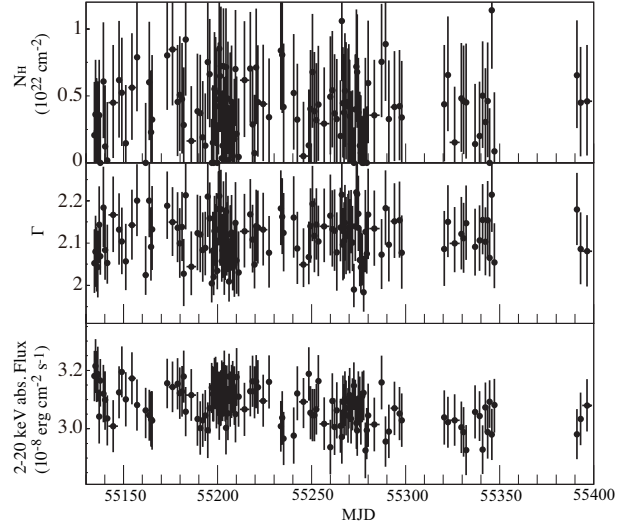


Fig. A-1. Best-fit values and statistical errors of absorbed power-law model to GSC Crab Nebula spectra against the observation time; (top) hydrogen column density, (middle) photon index, (bottom) 2–20 keV absorbed flux.

Table A-1. Best-fit values and variations of absorbed power-law model to GSC Crab Nebula spectra

Parameter	Canonical	Best fit	rms*
$N_{\text{H}} (\times 10^{22} \text{ cm}^{-2})$	0.35	0.39	0.25
Γ	2.10	2.11	0.05
Γ^\ddagger		2.11	0.03
$\text{Flux}_{2-20\text{keV}}^\dagger$	$3.0 \pm 10\%$	3.08	0.06

Notes.

* Root mean square of the best-fit value

† In unit of $10^{-8} \text{ erg s}^{-1} \text{ cm}^{-2}$

‡ N_{H} is fixed at $0.35 \times 10^{22} \text{ cm}^{-2}$